




## Article

# Sr Substituted $\text{La}_{2-x}\text{Sr}_x\text{Ni}_{0.8}\text{Co}_{0.2}\text{O}_{4+\delta}$ ( $0 \leq x \leq 0.8$ ): Impact on Oxygen Stoichiometry and Electrochemical Properties

Ifeanyichukwu D. Unachukwu <sup>1,2</sup>, Vaibhav Vibhu <sup>1,\*</sup> , Izaak C. Vinke <sup>1</sup>, Rüdiger-A. Eichel <sup>1,2</sup>  and L. G. J. (Bert) de Haart <sup>1</sup> 

<sup>1</sup> Institute of Energy and Climate Research, Fundamental Electrochemistry (IEK-9), Forschungszentrum Jülich GmbH, 52425 Jülich, Germany; i.unachukwu@fz-juelich.de (I.D.U.); i.c.vinke@fz-juelich.de (I.C.V.); r.eichel@fz-juelich.de (R.-A.E.); l.g.j.de.haart@fz-juelich.de (L.G.J.d.H.)

<sup>2</sup> Institute of Physical Chemistry, RWTH Aachen University, 52074 Aachen, Germany

\* Correspondence: v.vibhu@fz-juelich.de

**Abstract:** Lanthanide nickelate  $\text{Ln}_2\text{NiO}_{4+\delta}$  (Ln = La, Pr, or Nd) based mixed ionic and electronic conducting (MIEC) materials have drawn significant attention as an alternative oxygen electrode for solid oxide cells (SOCs). These nickelates show very high oxygen diffusion coefficient ( $D^*$ ) and surface exchange coefficient ( $k^*$ ) values and hence exhibit good electrocatalytic activity. Earlier reported results show that the partial substitution of  $\text{Co}^{2+}$  at B-site in  $\text{La}_2\text{Ni}_{1-x}\text{Co}_x\text{O}_{4+\delta}$  (LNCO) leads to an enhancement in the transport and electrochemical properties of the material. Herein, we perform the substitution at A-site with Sr, i.e.,  $\text{La}_{2-x}\text{Sr}_x\text{Ni}_{0.8}\text{Co}_{0.2}\text{O}_{4+\delta}$ , in order to further investigate the structural, physicochemical, and electrochemical properties. The structural characterization of the synthesized powders reveals a decrease in the lattice parameters as well as lattice volume with increasing Sr content. Furthermore, a decrease in the oxygen over stoichiometry is also observed with Sr substitution. The electrochemical measurements are performed with the symmetrical half-cells using impedance spectroscopy in the 700–900 °C temperature range. The total polarization resistance of the cell is increased with Sr substitution. The electrode reaction mechanism is also studied by recording the impedance spectra under different oxygen partial pressures. Finally, the kinetic parameters are investigated by analyzing the impedance spectra under polarization. A decrease in exchange current density ( $i_0$ ) is observed with increasing Sr content.

**Keywords:** nickelates; SOECs; SOFCs; oxygen over stoichiometry; chemical stability; electrochemical performance



**Citation:** Unachukwu, I.D.; Vibhu, V.; Vinke, I.C.; Eichel, R.-A.; de Haart, L.G.J. Sr Substituted  $\text{La}_{2-x}\text{Sr}_x\text{Ni}_{0.8}\text{Co}_{0.2}\text{O}_{4+\delta}$  ( $0 \leq x \leq 0.8$ ): Impact on Oxygen Stoichiometry and Electrochemical Properties. *Energies* **2022**, *15*, 2136. <https://doi.org/10.3390/en15062136>

Academic Editor: Paola Costamagna

Received: 15 February 2022

Accepted: 10 March 2022

Published: 15 March 2022

**Publisher's Note:** MDPI stays neutral with regard to jurisdictional claims in published maps and institutional affiliations.



**Copyright:** © 2022 by the authors. Licensee MDPI, Basel, Switzerland. This article is an open access article distributed under the terms and conditions of the Creative Commons Attribution (CC BY) license (<https://creativecommons.org/licenses/by/4.0/>).

## 1. Introduction

The increase in greenhouse gases due to fossil fuels, as well as the growing demand for energy, has resulted in a corresponding need for alternative energy sources. Among many possibilities, the solid oxide fuel cell (SOFC) remains a major alternative due to its high theoretical efficiency when compared with heat engines [1]. The SOFC can efficiently generate electricity while using hydrogen produced from the solid oxide electrolysis cells (SOECs). Furthermore, the SOFC can also accommodate the use of other fuels such as natural gas, methane, methanol, ethanol, and ammonia [2–5].

However, one of the major challenges is to mitigate the degradation rate and increase the widespread use of solid oxide cells, especially at high current densities during long-term operation [6,7]. In addition, the oxygen electrodes contribute more to the polarization resistance of single cells owing to the slow kinetics of the oxygen reduction reaction (ORR) [8,9]. Therefore, further modifications in the existing materials, as well as the search for new materials, are important in order to improve the oxygen transport properties, electrochemical activity, and durability of the cells. For the electrodes comprising purely electrical conductors, such as  $\text{La}_{1-x}\text{Sr}_x\text{MnO}_3$  (LSM), the oxygen reduction reaction mainly

occurs at the triple phase boundary (TPB) [10]. Therefore, mixed ionic and electronic conductors (MIEC) have gained much attention as oxygen electrodes due to their mixed conductivity, where the electrode reactions take place at the entire surface area of the MIEC electrode exposed to the gas phase as well as at the TPB [11,12]. The extension of the electrochemical reaction zone further results in an increase in the overall electrode activity.

There are mainly two kinds of MIEC materials that can be used as oxygen electrodes for SOCs. This classification is based on the defect mechanism through which they conduct oxide ions. The first type is related to oxygen-deficient materials such as  $\text{La}_{1-x}\text{Sr}_x\text{Co}_{1-y}\text{Fe}_y\text{O}_{3-\delta}$  (LSCF), in which the oxide ion conduction occurs through the oxygen vacancies present in their lattice structure [13–15]. The second type of MIEC electrode is based on oxygen over stoichiometry materials, e.g., lanthanide nickelates  $\text{Ln}_2\text{NiO}_{4+\delta}$  ( $\text{Ln} = \text{La}, \text{Pr}, \text{or Nd}$ ), in which the conduction of oxide ion takes place through oxygen interstitial sites [16–21].

So far, deficient perovskites have been extensively studied as oxygen electrodes [22–24]. Particularly, the current state-of-the-art LSCF oxygen electrode shows good ionic and electronic conductivity, more than the conventional LSM electrode which shows a predominant electronic conductivity [6,7]. However, this  $\text{Sr}^{2+}$ -containing electrode exhibits Sr-segregation as well as phase change from rhombohedral to cubic, which results in deterioration of the electrode performance, especially during long-term operation [22–24]. Therefore, to avoid such issues, lanthanide nickelates  $\text{Ln}_2\text{NiO}_{4+\delta}$  ( $\text{Ln} = \text{La}, \text{Pr}, \text{or Nd}$ ) based oxygen over stoichiometric materials with a  $\text{K}_2\text{NiF}_4$ -type structure are considered as an alternative oxygen electrode. These nickelates are particularly attractive owing to their high oxide ion diffusivity ( $D^*$ ), surface exchange kinetics ( $k^*$ ), as well as high electro-catalytic activity [16–18,25–27]. In principle, the defect chemistry of perovskites could affect the diffusivity and the transport kinetics of oxygen ions through the perovskite electrode. For example, the oxygen non-stoichiometry properties of perovskites (represented by their oxygen vacancies and interstitial sites) can enhance oxide ion transport through vacancy and interstitialcy mechanisms [28,29]. Such an effective increase in the oxygen ion transport through the electrode can improve electrochemical properties via the reduction in ion diffusion resistance [28–30].

Generally, the electrochemical properties of oxygen electrodes can be altered, in many cases enhanced, through the partial or complete substitution of the A-site or B-site element of the perovskite [13–18,31]. In the case of layered perovskites, recently it has been shown that the partial substitution at the B-site, i.e., Ni-site with cobalt in  $\text{La}_2\text{Ni}_{1-x}\text{Co}_x\text{O}_{4+\delta}$  ( $x = 0, 0.1, 0.2$ ), enhances the physicochemical properties of the materials and hence increases the electrochemical performance of the electrode [31–33]. For simple perovskites such as LSCF or LSC, the partial substitution of the  $\text{La}^{3+}$  with  $\text{Sr}^{2+}$  at the A-site leads to an increase in the electronic/ionic conductivity and hence enhances the overall electrochemical properties [34,35]. In this work, we have considered the same strategy, i.e., Sr substitution at the La-site, to further modify the properties of the layered perovskite  $\text{La}_2\text{Ni}_{0.8}\text{Co}_{0.2}\text{O}_{4+\delta}$ . Six compositions are mainly considered, i.e.,  $\text{La}_{2-x}\text{Sr}_x\text{Ni}_{0.8}\text{Co}_{0.2}\text{O}_{4+\delta}$  ( $x = 0$ , LNC0;  $x = 0.05$ , LSNCO5;  $x = 0.1$ , LSNCO10;  $x = 0.2$ , LSNCO20;  $x = 0.4$ , LSNCO40;  $x = 0.8$ , LSNCO80). The steps involve the synthesis of  $\text{La}_{2-x}\text{Sr}_x\text{Ni}_{0.8}\text{Co}_{0.2}\text{O}_{4+\delta}$  (LSNCO) materials, followed by their structural and physicochemical characterizations. Finally, the electrochemical characterization of these materials is carried out by fabricating symmetrical half-cells.

## 2. Experimental

### 2.1. Powder Preparation

All  $\text{La}_{2-x}\text{Sr}_x\text{Ni}_{0.8}\text{Co}_{0.2}\text{O}_{4+\delta}$  (LSNCO) phases ( $0.0 \leq x \leq 0.8$ ) were prepared using the citrate–nitrate route (modified Pechini method) [36]. The precursors are  $\text{La}_2\text{O}_3$  (Sigma Aldrich, Saint Louis, MO, USA, 99.9%),  $\text{SrCO}_3$  (Sigma Aldrich, 99.9%),  $\text{Ni}(\text{NO}_3)_2 \cdot 6\text{H}_2\text{O}$  (Alfa Aesar, Haverhill, MA, USA, 99%), and  $\text{Co}(\text{NO}_3)_2 \cdot 6\text{H}_2\text{O}$  (Alfa Aesar, 99%).  $\text{La}_2\text{O}_3$  was pre-fired at 900 °C overnight to remove the water content, due to the high hygroscopic character. The exact amount of the precursors was gradually dissolved in dilute nitric acid

one after the other (solution of 10 mL of  $\text{HNO}_3$  (65%) and 20 mL of water). A 10% molar excess of citric acid was added to the solution. The solution was then heated on a hot plate (about 110 °C) with continuous stirring with a magnetic stirrer until a viscous gel was formed. This was followed by auto combustion at about 300 °C. The final annealing was performed at 1300 °C for 12 h in the air to obtain well-crystallized phases.

## 2.2. X-ray Diffraction Analysis

The powders were analyzed using X-ray diffraction (XRD) at room temperature. A PANalytical X'pert MPD diffractometer with  $\text{Cu-K}\alpha$  incident radiation was used for the characterization. The lattice parameter and lattice volume were determined by Rietveld analysis of the X-ray diffractogram using FullProf Software (Grenoble, France).

## 2.3. Microstructural Analysis

The morphologies of the powders as well as the cells were analyzed using a scanning electron microscope (Quanta FEG 650, Hillsboro, OR, USA, FEI equipped with an EDX detector). During the sample preparation for SEM, the powdered samples were distributed on carbon tape to avoid charging effects during the analyses.

## 2.4. Thermo-Gravimetric Analysis (TGA)

TGA analyses of the as-prepared powders were carried out by using a TA-Q5500 thermogravimetric analyzer. In the first step, the powdered samples were cycled three times from 50 to 1000 °C. The first cycle was completed in the air to equilibrate the system. The second cycle was also carried out in the air to determine the reversibility of oxygen uptake/release in the sample. A heating rate of 2 °C/min was used for the first two cycles. The third cycle was carried out under  $\text{Ar-4\% H}_2$  (with a slow heating rate of 0.5 °C/min) to determine the value of the oxygen over stoichiometry ( $\delta$ -value) at room temperature. The variation of the oxygen over stoichiometry as a function of temperature (in the air) could be obtained from the second cycle. In another step, the powders were cycled four times at 2 °C/min from 50 to 1000 °C. The first two cycles were under air, and the final two were under an oxygen atmosphere. This step aims to determine the change in oxygen over stoichiometry under an oxygen atmosphere.

## 2.5. Cell Preparation and Fabrication

First, the screen-printing pastes of LSNCO were prepared by mixing the powders in a solution of  $\alpha$ -terpineol and ethyl cellulose. The paste was mixed with a planetary vacuum mixer (THINKY Mixer ARV-310) followed by roll milling for 30 min to ensure a homogenous mixture.

The symmetrical half-cells were then prepared by using dense 8YSZ electrolyte support from Kerafol® (diameter ~20 mm, thickness ~300  $\mu\text{m}$ ). At first, a thin layer (~4–5  $\mu\text{m}$ ) of GDC was screen printed (M2-H, EKRA screen printing Technologies) on both sides of 8YSZ substrates as a barrier layer (sintered at 1350 °C for 1 h under air). After drying, the nickelate layer (diameter ~10 mm, thickness ~15–20  $\mu\text{m}$ ) was screen printed on each side. The symmetrical half-cell structure can be represented as electrode//GDC//8YSZ//GDC//electrode. After the fabrication, the sintering temperature was optimized using an LNCO electrode containing symmetrical half-cells. Three different sintering temperatures i.e., 1100, 1150, and 1200 °C for 1 h were considered. Among them, 1150 °C for 1 h was selected as an optimized sintering condition based on the polarization resistance (Supplementary Materials, Figure S1).

## 2.6. Electrochemical Characterization

The electrochemical measurements were performed with symmetrical half-cells in the 700–900 °C temperature range, using the electrochemical impedance spectroscopy (EIS) technique. All impedance diagrams were recorded under potentiostatic control with a 50 mV ac amplitude, from 1.1 MHz down to 0.11 Hz, using an IVIUM VERTEX

potentiostat/galvanostat (Ivium Technologies BV, Eindhoven, The Netherlands) with an integrated frequency response analyzer module. Two types of measurements were carried out; the first one was carried out at open-circuit voltage (OCV) conditions in air and under different oxygen partial pressures using a two-electrode four wire setup. These measurements were performed in order to determine the electrode polarization resistance ( $R_p$ ), the oxygen electrode reaction mechanism, as well as the rate-limiting step among the involved processes. The second measurement was carried out under polarization (+0.2 V to −0.2 V) using a three-electrode setup. A Pt point electrode was attached at the edge of the 8YSZ electrolyte, acting as the reference electrode, while the top and bottom parts of the cell act as the working and counter electrodes, respectively. These measurements were performed in order to determine the kinetic parameters such as exchange current density ( $i_0$ ) and exchange coefficient ( $\alpha$ ). All impedance diagrams were fitted using an equivalent circuit model by means of the RelaxIS<sup>®</sup> (RHD-Instruments, Darmstadt, Germany) software, V 3.0. 18. 15.

### 3. Results and Discussion

#### 3.1. X-ray Diffraction Analyses

The XRD analyses of as-prepared powders indicate that all these materials exist in single phases. Figure 1 represents the FullProf refinement of the as-synthesized powders of LSNCO5, LSNCO10, and LSNCO20, as an example. A good match between experimental and refined diffraction patterns is observed. This could be validated from the corresponding chi-square values, which describe the quality of the Rietveld refinement. The diffraction patterns show complete crystallization of the powders as a single-phase in the  $K_2NiF_4$ -type structure across the entire composition range ( $0.0 \leq x \leq 0.8$ ). The peaks of  $La_{2-x}Sr_xNi_{0.8}Co_{0.2}O_{4+\delta}$  with  $x \leq 0.05$  were indexed with an orthorhombic cell structure described by the  $Fmmm$  space group, while the composition of  $0.05 < x \leq 0.8$  were indexed with a tetragonal cell described by the  $F4/mmm$  space group. A phase transition from orthorhombic to tetragonal is observed with increasing Sr content for  $x > 0.05$ . It is suspected that the amount of Sr in  $x \leq 0.05$  was not sufficient to cause a pronounced structural transition.

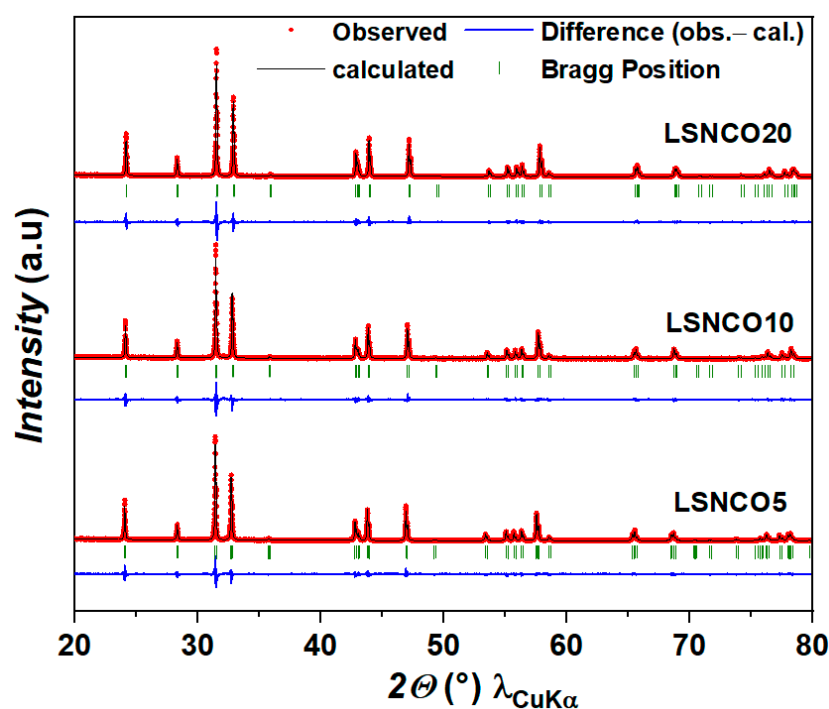


**Figure 1.** FullProf refinement of the X-ray diffraction patterns of LNC05 ( $\chi^2 = 2.12$ ), LSNCO10 ( $\chi^2 = 2.70$ ), and LSNCO20 ( $\chi^2 = 2.51$ ).

Furthermore, the lattice parameters were also determined from the FullProf profile matching and are shown in Figure 2a. A decrease in lattice parameters  $a$  and  $b$  is observed with increasing Sr content. For example, the lattice parameter  $a$  is decreased from 5.461 for  $x = 0.1$  to 5.395 for  $x = 0.8$ . The lattice parameter  $c$  is initially increased from  $x = 0$  to  $x = 0.4$ , followed by a steep decrease up to  $x = 0.8$ . However, a continuous decrease in the cell volume is observed with increasing Sr content, as depicted in Figure 2b.

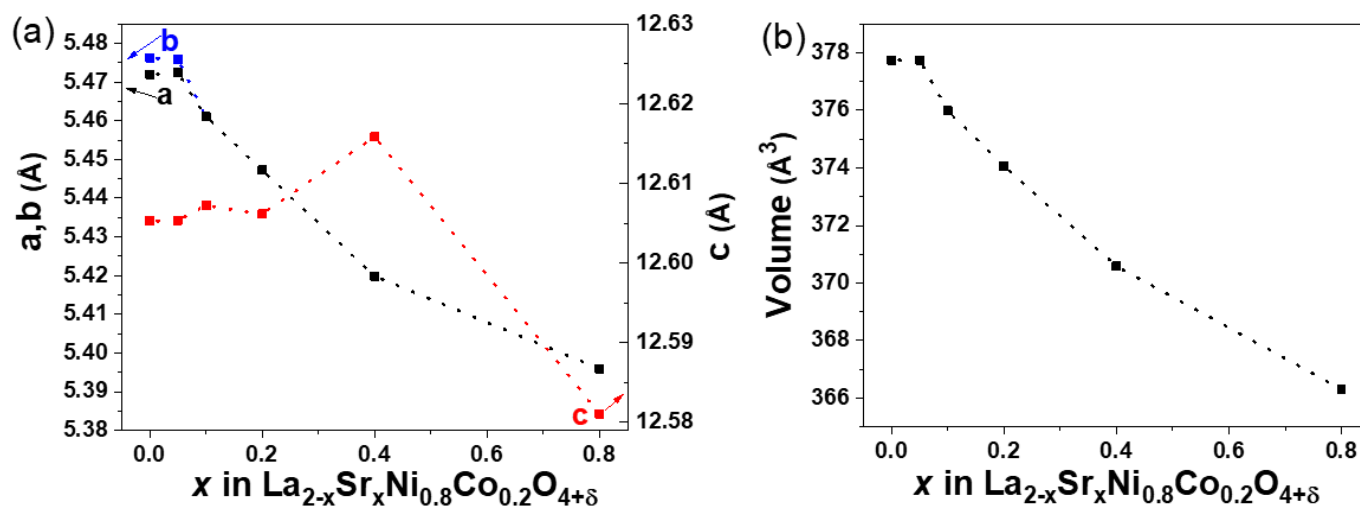


**Figure 2.** (a) Variation of lattice parameters  $a$ ,  $b$ , and  $c$ , and (b) variation of the cell volume as a function of Sr substitution for  $\text{La}_{2-x}\text{Sr}_x\text{Ni}_{0.8}\text{Co}_{0.2}\text{O}_{4+\delta}$  compounds.

Usually, the substitution at the A-site with another cation of different valence leads to a charge imbalance. Therefore, to maintain charge neutrality, the extra charge can be compensated in two ways; either by the creation of oxygen vacancies or by increasing the charge of a multivariate B-site cation [37]. However, for  $\text{K}_2\text{NiF}_4$ -type nickelates, the charge balance often occurs by increasing the oxidation number of nickel from  $\text{Ni}^{2+}$  to  $\text{Ni}^{3+}$  [38,39]. A similar result is expected for  $\text{La}_{2-x}\text{Sr}_x\text{Ni}_{0.8}\text{Co}_{0.2}\text{O}_{4+\delta}$ . Since the size of  $\text{Ni}^{3+}$  (0.60 Å) is smaller than that of  $\text{Ni}^{2+}$  (0.69 Å), therefore, increasing  $\text{Ni}^{3+}$  content with increasing Sr substitution leads to a decrease in the overall cell volume. In addition, the increase in  $\text{Ni}^{3+}$  content leads to a decrease in the Ni–O bond length, which further results in a decline in the lattice parameter  $a$  and  $b$  [38,40]. The initial increase in lattice parameter  $c$  could be attributed to the difference in the ionic radius of  $\text{La}^{3+}$  and  $\text{Sr}^{2+}$ .  $\text{Sr}^{2+}$  has a larger ionic radius (1.27 Å) in comparison with  $\text{La}^{3+}$  (1.16 Å), resulting in the increase in lattice parameter  $c$  with an increase in  $\text{Sr}^{2+}$  content. This is in agreement with other reports in the literature [38–42]. However, for higher contents of Sr, ( $x > 0.4$ ), a decrease in lattice parameter  $c$  was observed which also contributed to a general decrease in cell volume. This steep decline in lattice parameter  $c$  can be attributed to structural instability of the perovskite as a result of the Jahn–Teller distortion [38,39].

### 3.2. Thermogravimetric Analyses

The oxygen over stoichiometry ( $\delta$ -value) of all LSNCO compounds was determined by performing TGA experiments under reducing conditions ( $\text{Ar}-4\% \text{H}_2$  atmosphere, with a slow heating rate of  $0.5^\circ\text{C}\cdot\text{min}^{-1}$ ) after the samples were equilibrated in air. The weight loss (in %) as a function of temperature for LNCO, LSNCO5, and LSNCO10 powders are shown in Figure 3a, as an example. All the powders followed the same temperature variation pattern and show mainly two-weight losses, similar to previously reported results for other  $\text{K}_2\text{NiF}_4$ -type nickelates [16,31,43]. The first weight loss occurs at around  $400^\circ\text{C}$ , which corresponds to the loss of oxygen over stoichiometry. The second weight loss between  $600$  and  $700^\circ\text{C}$  represents the complete reduction in the powders to their appropriate ratio. For instance, in the case of LSNCO10, the first transition involves a

reduction from  $\text{La}_{1.9}\text{Sr}_{0.1}\text{Ni}_{0.8}\text{Co}_{0.2}\text{O}_{4+\delta}$  to  $\text{La}_{1.9}\text{Sr}_{0.1}\text{Ni}_{0.8}\text{Co}_{0.2}\text{O}_4$ . The second weight loss involves a reduction from  $\text{La}_{1.9}\text{Sr}_{0.1}\text{Ni}_{0.8}\text{Co}_{0.2}\text{O}_4$  to  $0.95\text{La}_2\text{O}_3 + 0.10\text{SrO} + 0.8\text{Ni} + 0.2\text{Co}$ , as confirmed by the XRD (Supplementary Materials, Figure S2).

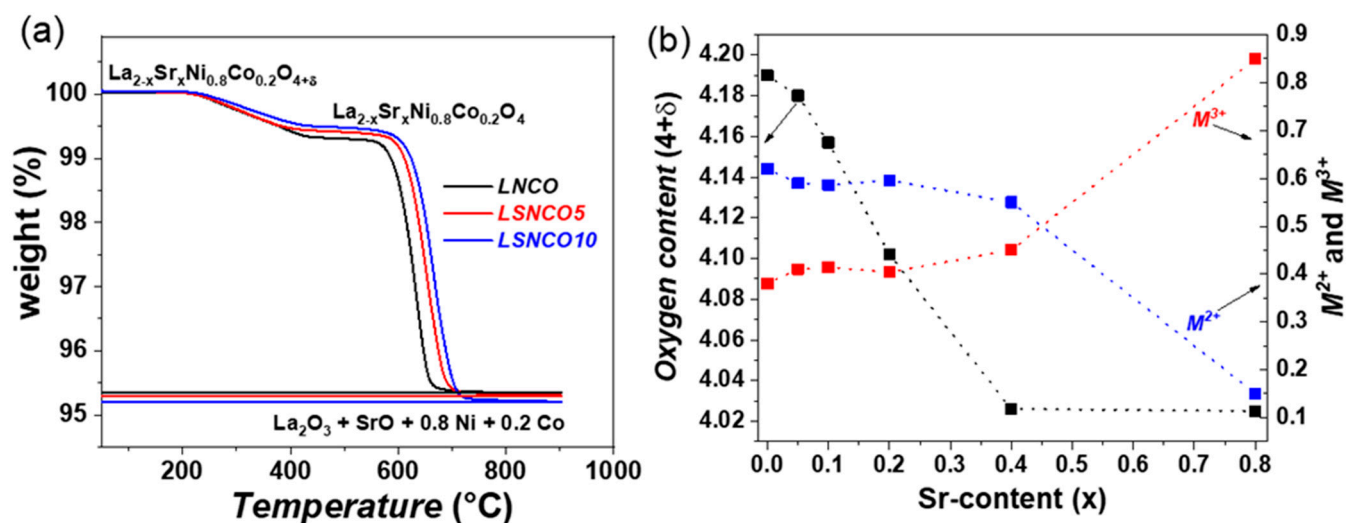


**Figure 3.** (a) Weight loss curve under Ar-4%  $\text{H}_2$  atmosphere and (b) thermal variation of the oxygen over stoichiometry ( $\delta$ -value) as well as the  $M^{2+}$  ( $\text{Ni}^{2+}/\text{Co}^{2+}$ ) and  $M^{3+}$  ( $\text{Ni}^{3+}/\text{Co}^{3+}$ ) content of  $\text{La}_{2-x}\text{Sr}_x\text{Ni}_{0.8}\text{Co}_{0.2}\text{O}_{4+\delta}$  compounds.

The delta ( $\delta$ ) values of all LSNCO compositions are listed in Table 1. A continuous decrease in the  $\delta$  value from 0.19 (LNCO) to 0.025 (LSNCO80) is observed with increasing Sr substitution, as shown in Figure 3b. The obtained  $\delta$ -value for LNCO is in agreement with the earlier reported results [31,33]. The amount of  $M^{3+}$  ( $\text{Ni}^{3+}/\text{Co}^{3+}$ ) is also increased, an especially large increase is observed for  $x \geq 0.2$  (Figure 3b). Therefore, the decrease in the  $\delta$  value with increasing Sr implies a decrease in the interstitial oxygen sites. The decreasing oxygen content of LSNCO indicates that the oxygen ion transport properties of the material are decreasing with increasing Sr substitution, and it is also in good agreement with the previously reported results for the Sr-substituted  $\text{La}_2\text{NiO}_{4+\delta}$  materials [44].

**Table 1.** Oxygen over stoichiometry ( $\delta$ -value) calculated from TGA for  $\text{La}_{2-x}\text{Sr}_x\text{Ni}_{0.8}\text{Co}_{0.2}\text{O}_{4+\delta}$  compounds.

Phase Composition	$\delta$ -Value
$\text{La}_2\text{Ni}_{0.8}\text{Co}_{0.2}\text{O}_{4+\delta}$ (LNCO)	0.19
$\text{La}_{1.95}\text{Sr}_{0.05}\text{Ni}_{0.8}\text{Co}_{0.2}\text{O}_{4+\delta}$ (LSNCO5)	0.18
$\text{La}_{1.9}\text{Sr}_{0.1}\text{Ni}_{0.8}\text{Co}_{0.2}\text{O}_{4+\delta}$ (LSNCO10)	0.16
$\text{La}_{1.8}\text{Sr}_{0.2}\text{Ni}_{0.8}\text{Co}_{0.2}\text{O}_{4+\delta}$ (LSNCO20)	0.10
$\text{La}_{1.6}\text{Sr}_{0.4}\text{Ni}_{0.8}\text{Co}_{0.2}\text{O}_{4+\delta}$ (LSNCO40)	0.03
$\text{La}_{1.2}\text{Sr}_{0.8}\text{Ni}_{0.8}\text{Co}_{0.2}\text{O}_{4+\delta}$ (LSNCO80)	0.02

Figure 4a,b illustrate the thermal variation of the oxygen content for LSNCO compounds under air and under oxygen atmospheres, respectively. All the compositions exhibit a reversible oxygen exchange and maintain oxygen over stoichiometry across the entire temperature range in both air and oxygen atmospheres. In an oxygen atmosphere, the uptake of oxygen is observed and leads to an increase in oxygen over stoichiometry. For instance, the oxygen over stoichiometry value of LSNCO5 and LSNCO10 increased from 0.18 and 0.16 in an air atmosphere to 0.23 and 0.20 in the oxygen atmosphere, respectively. For LSNCO40, almost no change in the oxygen content is observed during heating and cooling under both atmospheres.



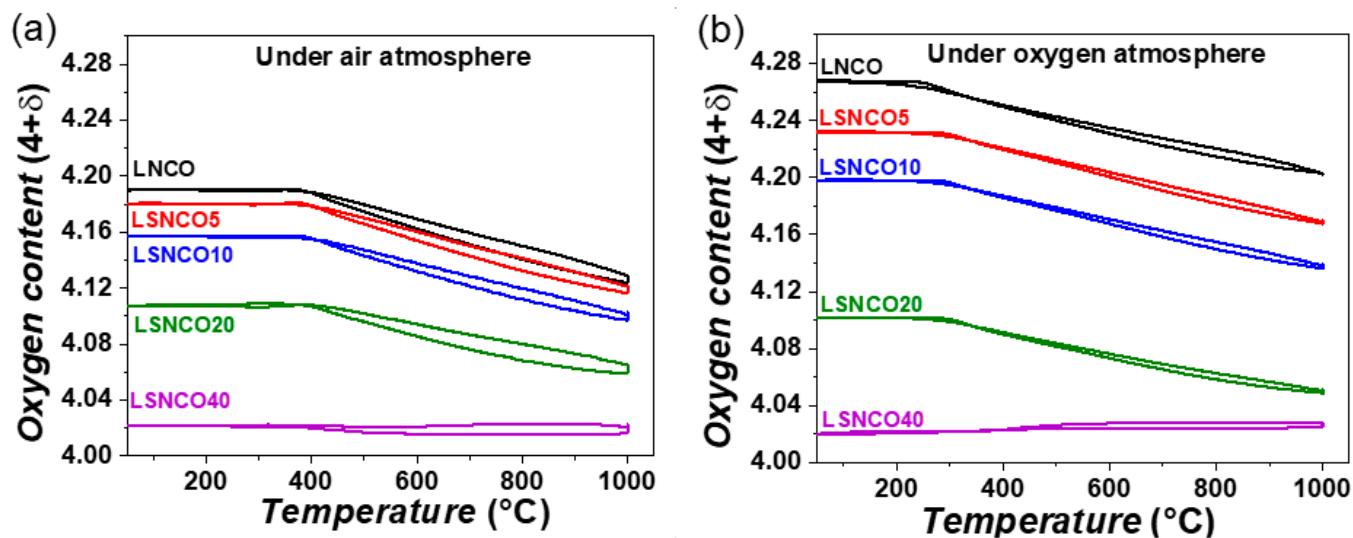


**Figure 4.** Variation of oxygen over stoichiometry as a function of temperature ( $50 \leq T \leq 1000$  °C): (a) under air atmosphere and (b) under oxygen atmosphere.

### 3.3. Reactivity Test

The chemical reactivity tests between LSNCO and GDC were separately performed at the sintering temperature of the cell, with the aim to investigate the thermal stability and compatibility. In this respect, the powders of all LSNCO compositions were considered and mixed with GDC in the ratio of 50:50 and sintered at 1150 °C for 1 h. The resulting powders were analyzed by XRD and the corresponding diffractograms are depicted in Figure 5.

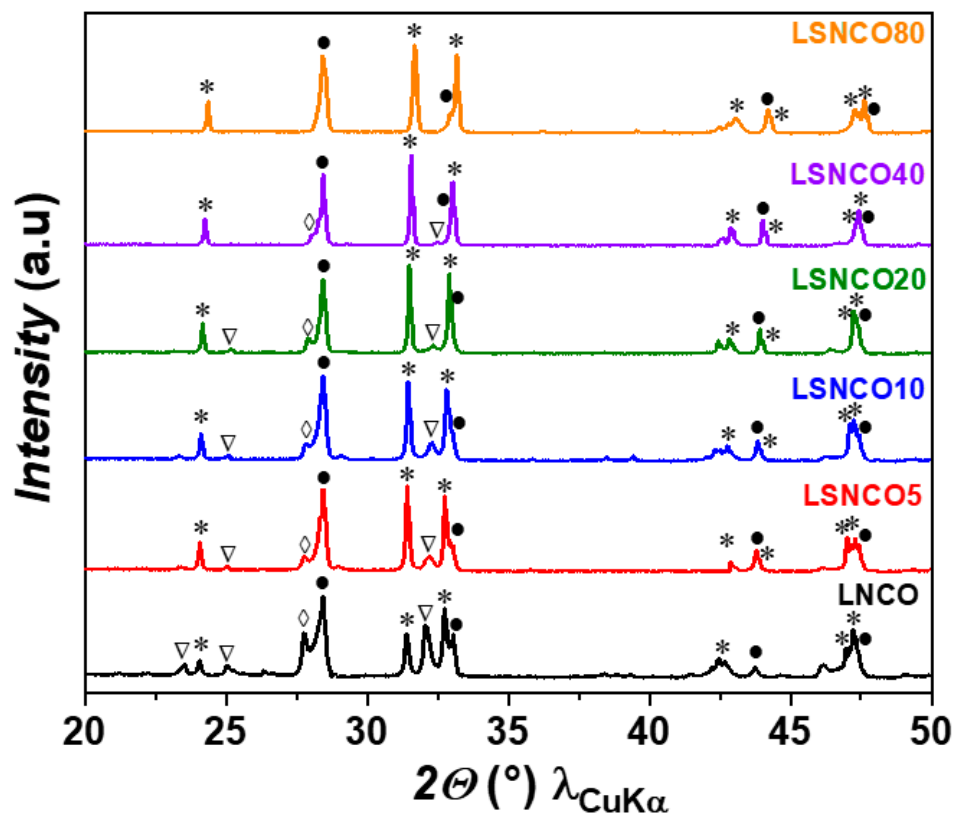


**Figure 5.** X-ray diffractograms of the LSNCO phases mixed with GDC (in the ratio of 50:50) at 1150 °C/1 h. LSNCO (\*), GDC/(La,Gd)CeO<sub>2</sub> (•), La<sub>2</sub>Ce<sub>2</sub>O<sub>7</sub> (◇), and La<sub>3</sub>(Ni,Co)<sub>2</sub>O<sub>7</sub> (▽).

The LNCO material is not compatible with the GDC, as various phases including LNCO,  $\text{La}_2\text{Ce}_2\text{O}_7$ ,  $(\text{La,Gd})\text{CeO}_2$ , and  $\text{La}_3(\text{Ni,CO})_2\text{O}_7$  were detected. These phases are in good agreement with the earlier reported results [31]. The earlier reported results show that the reactivity between LNCO and GDC takes place mainly at the sintering temperature due to the interdiffusion of cations, while at the operating temperature, i.e., (800 °C/24 h), no reactivity is observed. However, interestingly, with increasing Sr content the reactivity with GDC is decreased, and for LSNCO80, no reactivity is observed.

### 3.4. Powder Morphology

The as-synthesized powders of all LSNCO compounds were investigated using SEM, with special attention to the particle/grain size. Usually, smaller particle sizes are desirable for electrode preparation due to the increased surface area, which provides more electrochemical reaction sites leading to a decrease in the polarization resistance [42,45]. The SEM images of as-synthesized powders of LSNCO5, LSNCO10, LSNCO20, and LSNCO40 are shown in Figure 6a,c,e,g, as an example. The particle sizes are in the order of several micrometers and big agglomerates are formed, mainly due to the high calcination temperature of the powders. Such pronounced particle agglomeration can reduce the electrode porosity as well as the electrode surface reaction area [42,45]. Hence, to reduce the particle clusters, the phase pure powders were further milled for an additional four hours at 250 rpm with zirconium balls and isopropanol. The SEM images of milled powders of LSNCO5, LSNCO10, and LSNCO20 are shown in Figure 6b,d,f,h, and confirm a particle size of  $\approx 1\text{--}2\text{ }\mu\text{m}$  for all compositions. These results are in agreement with the previously reported results for LNCO [31].

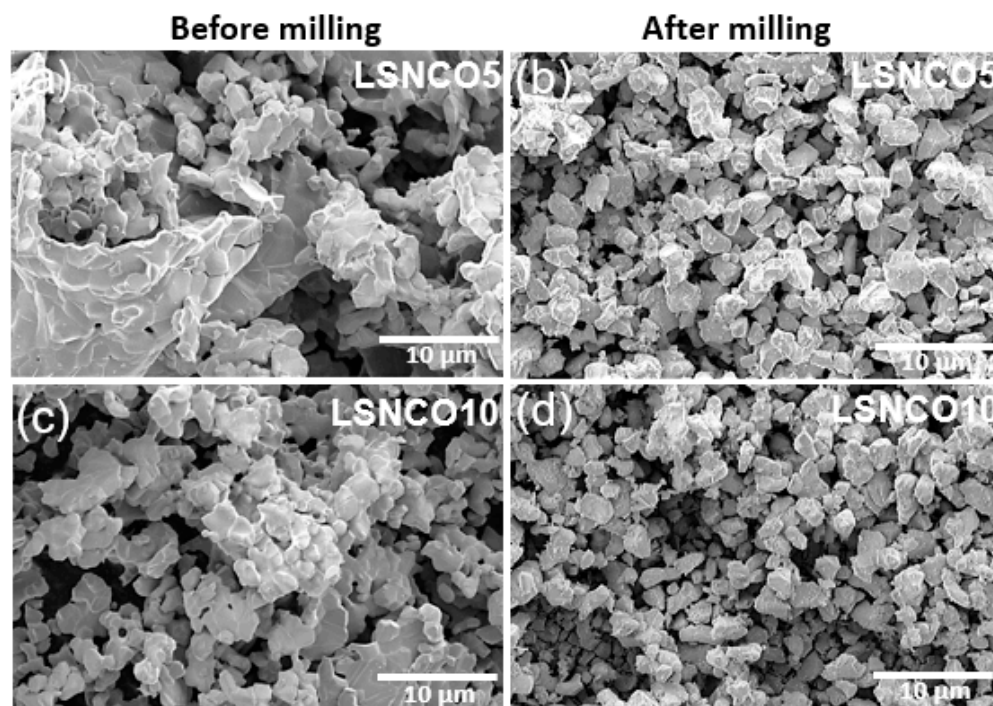
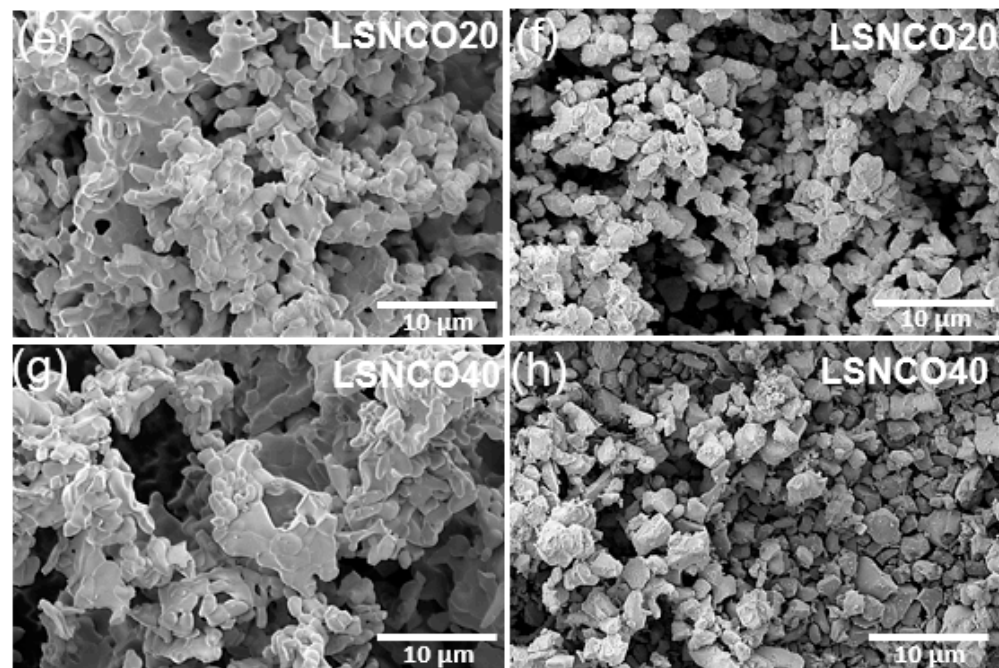


Figure 6. Cont.





**Figure 6.** SEM images of as-prepared powders of LSNCO5, LSNCO10, LSNCO20, and LSNCO40 (a,c,e,g) and after 4 h milling (b,d,f,h).

### 3.5. Electrochemical Characterizations of Symmetrical Half-Cells

The electrochemical properties of the symmetrical half-cells were investigated by impedance spectroscopy. For that, the symmetrical half-cell was mounted into the measurement setup with a flow of compressed air and the cell was heated at 900 °C. The impedance diagrams were investigated at  $i_{dc} = 0$  conditions in the temperature range of 700–900 °C under air. Distribution of relaxation time (DRT) analyses of impedance data were first performed in order to investigate the number of time constants. Figure S3 in the Supplementary Materials, represents the DRT plots of the LSNCO5, LSNCO10, and LSNCO20 symmetrical half-cells at 800 °C. Four peaks are observed for LSNCO5 and LSNCO10, however, for higher Sr content, mainly three peaks are observed. Therefore, the impedance spectra were fitted by an equivalent circuit model, either with four or three  $R//CPE$  (constant phase element) in series along with a series resistance  $R_s$ , depending on the composition.

The impedance diagrams with fitting are shown in Figure 7 for LSNCO5, LSNCO10, and LSNCO20 symmetrical half-cells. The total polarization resistances ( $R_p$ ) were obtained by adding the resistances associated with each time constant in an equivalent circuit. The variations of total  $R_p$  for LSNCO5, LSNCO10, and LSNCO20 electrodes as a function of  $T$  (Arrhenius plot) under OCV conditions, are shown in Figure 8. For all symmetrical half-cells, as expected,  $R_p$  decreases with an increase in temperature due to the thermally activated kinetics.

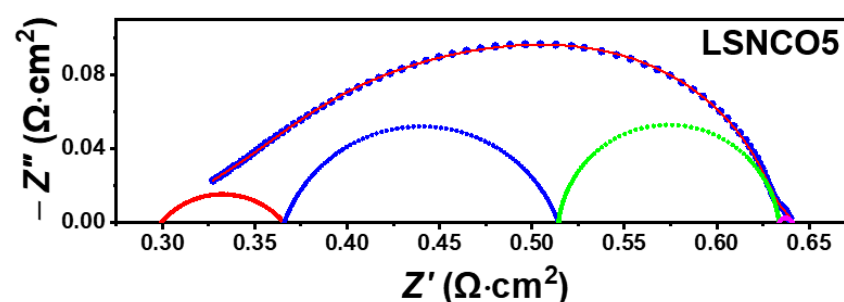


**Figure 7.** Cont.

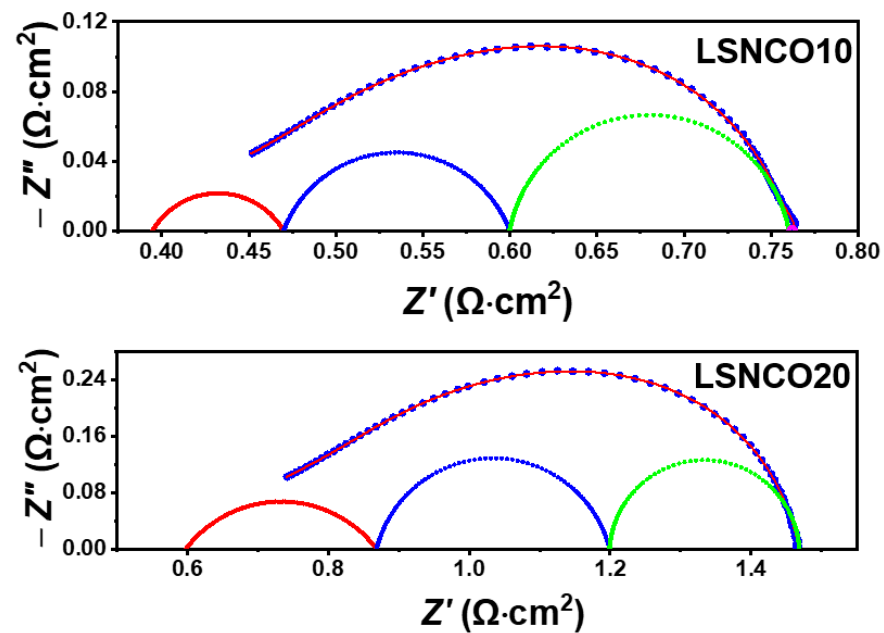


**Figure 7.** Impedance spectra and their fitting for LSNCO5, LSNCO10, and LSNCO20 symmetrical half-cells at 800 °C under OCV conditions.

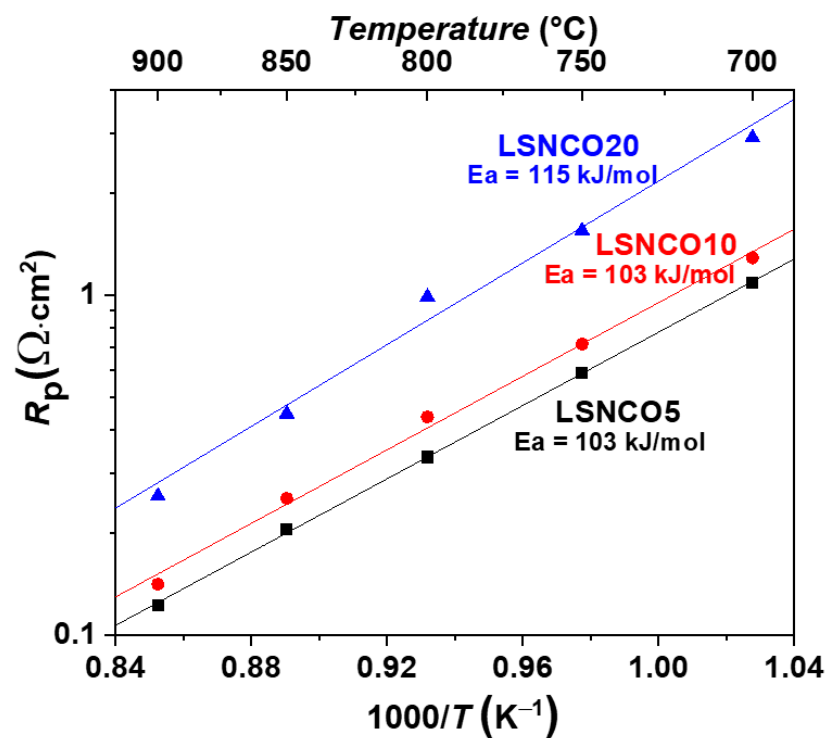


**Figure 8.** Compositional variation of  $R_p$  as a function of temperature under OCV conditions for symmetrical half-cells composed of LSNCO electrodes.

Moreover, an increase in  $R_p$  is observed with increasing Sr content. For instance, at 800 °C, the  $R_p$  values of LSNCO5, LSNCO10, and LSNCO20 are found to be 0.33, 0.44, and 1.13  $\Omega\cdot\text{cm}^2$ , respectively. This shows that the value of the  $R_p$  for LSNCO20 symmetrical half-cells is more than thrice the value of LSNCO5 at the same temperature. These values are even higher than that of the LSCO symmetrical half-cell, which shows a  $R_p$  value of 0.09  $\Omega\cdot\text{cm}^2$  at 800 °C [31]. With the increase in  $R_p$ , the result indicates that the electrochemical activity of the material is decreased with Sr substitution.

### 3.5.1. Mechanism of Oxygen Reduction Reaction and the Determination of Rate-Limiting Step

To investigate the effect of Sr substitution on the electrode reaction mechanism, the impedance measurements were performed under different oxygen partial pressures between 700 and 900 °C at OCV conditions. The variations of impedance spectra for the LSNCO5 symmetrical half-cell under different oxygen partial pressures from 0.06 atm to 0.98 atm, at 800 °C, are shown in Figure 9a, and corresponding DRT plots are shown in Figure 9b. In the DRT plots, four major peaks (P1, P2, P3, and P4) are mainly detected. The process P1 is independent of  $pO_2$ . This indicates a gas diffusion process. However, the other processes are varying with  $pO_2$ .

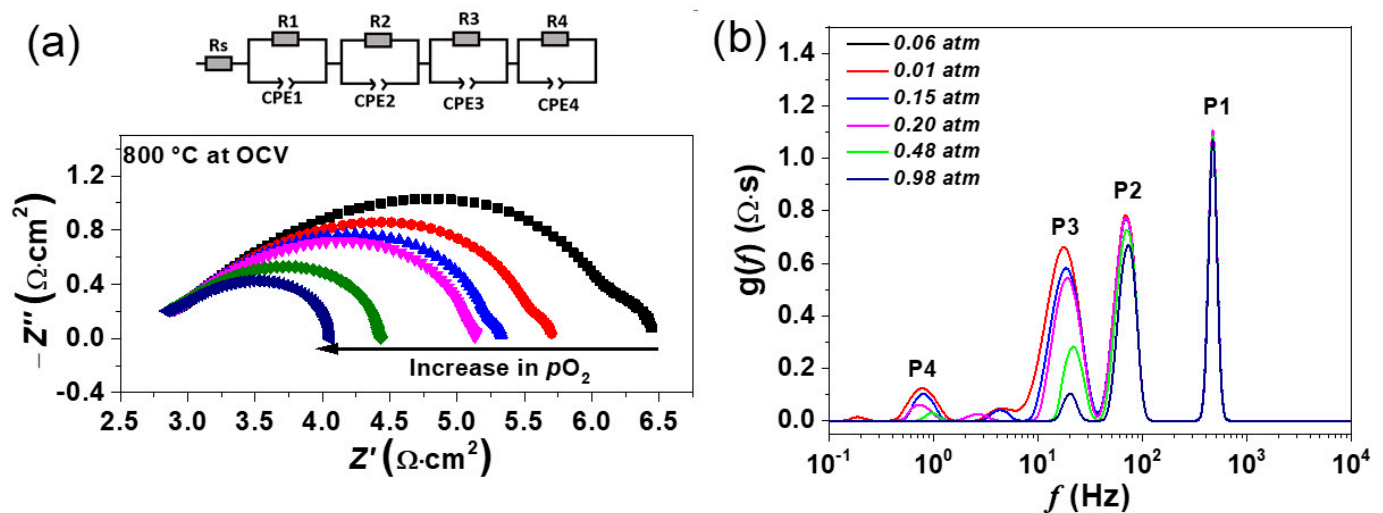


Figure 9. (a) Impedance spectra and (b) the DRT plots as a function of  $pO_2$  for LSNCO5 at 800 °C.

In order to calculate the polarization resistances of different processes, the impedance spectra were fitted with four R//CPE elements connected to a series resistance  $R_s$  for the LSNCO5 and LSNCO10 symmetrical half-cells. The impedance spectra of the LSNCO20 symmetrical half-cell were fitted with three R//CPE elements connected to a series resistance  $R_s$ .

In general, the polarization resistance of each electrode process is highly dependent on the oxygen partial pressure, as ascribed by Equation (1).

$$R_p \propto (pO_2)^{-m} \quad (1)$$

The exponent,  $m$ , gives information about the step involved in the oxygen evolution reaction [31,46,47].

For instance, when the value of the slope,  $m = 1$ , this indicates that molecular oxygen is involved in the process. It can be diffusion of  $O_2$  (g) on the surface and in the pores of the electrode and/or the adsorption of  $O_{2,ads}$  at the active reaction sites according to the following relation:



When the value of the slope,  $m = 0.5$ , this entails that atomic oxygen is involved in the reduction process. It can be interpreted as the dissociation of adsorbed molecular oxygen ( $O_{2,ads}$ ) into atomic species ( $O_{ads}$ ) at the electroactive sites of the MIEC oxide.



When the value of  $m = 0.25$ , this reveals that surface exchange reaction or charge transfer processes are involved, normally occurring at a two-phase gas–electrode interface.





When the value of the slope,  $m = 0$ , this corresponds to the ionic transfer of  $O^{2-}$  ions through the electrode–electrolyte interface as well as the diffusion of  $O^{2-}$  ions in the bulk of the electrode [31,48,49].



The variation of polarization resistances of the individual process, i.e., R1, R2, R3, and R4 as a function of  $pO_2$  at 800 °C are shown in Figure 10, for LSNCO5, LSNCO10, and LSNCO20. After performing the linear fit of individual resistances, four slope ( $m$ ) values are observed for LSNCO5 and LSNCO10, however, three slope ( $m$ ) values are obtained for LSNCO20. For example, the values of  $m$  for the LSNCO5 symmetrical half-cell are 0.09, 0.29, 0.49, and 1.08 for R1, R2, R3, and R4, respectively (Figure 10a). Similar  $m$  values are also observed for LSNCO10 (Figure 10b). For LSNCO20, three slopes values, i.e., 0.06, 0.25, and 0.48 are observed for R1, R2, and R3, respectively. Therefore, the value of  $m$  for R1 corresponds to the ionic transfer of  $O^{2-}$  ions across the electrode–electrolyte interface. R2 represents the charge transfer process, R3 corresponds to the adsorption/desorption of the atomic species into the molecular  $O_{2,ads}$  at the electroactive site of the electrode. Lastly, R4 illustrates the gas diffusion process, however, this process is not observed with higher Sr content, i.e., the LSNCO20 symmetrical half-cell due to the large contribution of other processes, which are obscuring the contribution of the low-frequency process within the impedance spectra.

It is worth mentioning that similar electrode processes are observed at 900 °C. For instance, the slope values for LSNCO5 are shown in the Supplementary Materials, Figure S4a. At a lower temperature, i.e., at 700 °C (Figure S4b), the processes corresponding to R1, R2, and R3 are maintained similar to 800 °C or 900 °C, however, the molecular gas diffusion process is not observed. Rather, another ionic transfer of the  $O^{2-}$  process corresponding to R4 ( $m \sim 0.09$ ) appeared at a lower temperature, which can be related to the diffusion of oxide ions through the bulk of the electrode. A similar result was observed by Kol'chugin et al. on doping LSCO with Sr ( $La_{1.7}Sr_{0.3}NiO_{4+\delta}$ ). They opined that the pronounced decrease in oxygen interstitial content resulted in the impeding of the cooperative oxygen-transfer mechanism, thereby leading to two different oxide ion migration channels; the first channel corresponding to a residual  $O^-$  migration through the interstitial while the second channel is the migration through oxygen vacancy of the perovskite layer [50]. Furthermore, Munnings et al. [32] and Boehm et al. [19] proposed an oxygen ionic diffusion mechanism involving both  $O^{2-}$  and  $O^-$  in LNO layered perovskites.

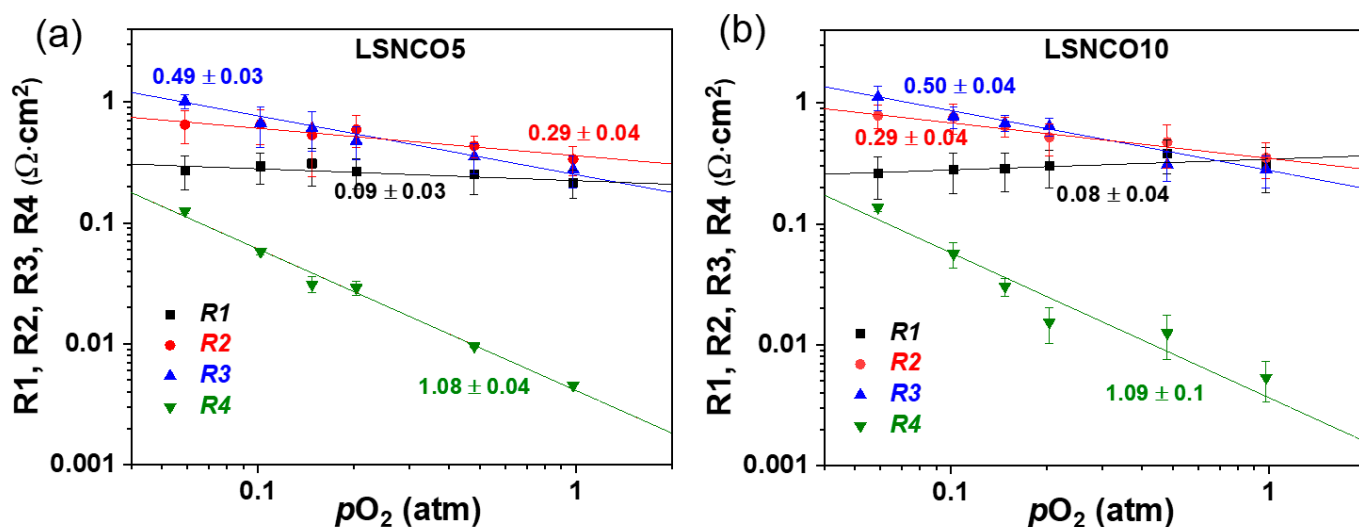
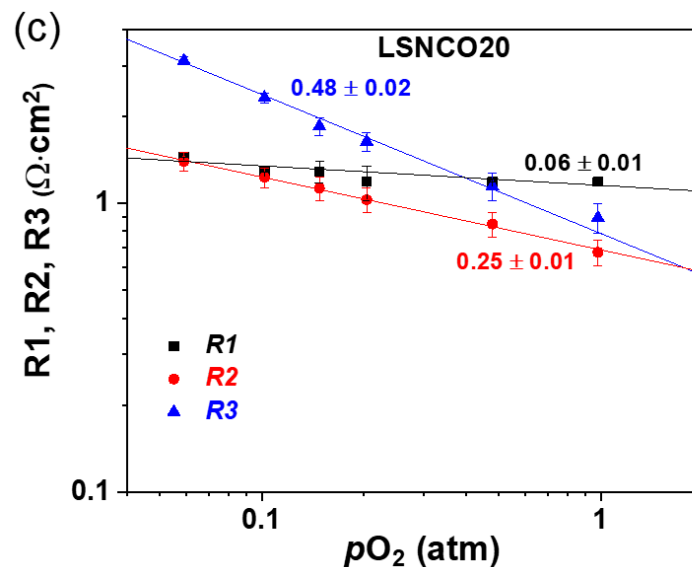


Figure 10. Cont.



**Figure 10.** Variation of R1, R2, R3, and R4 as a function of  $pO_2$  for (a) LSNCO5, (b) LSNCO10, and (c) LSNCO20 at 800 °C.

The rate-limiting step among all the electrode processes corresponds to the process that has the highest polarization resistance. Across the 700–900 °C temperature range, for LSNCO5, the adsorption/desorption of atomic species (R3) represents the rate-limiting step at low  $pO_2$ . However, at a higher  $pO_2$ , the rate-limiting step is dominated by the charge transfer process at 900 °C and 800 °C, while at 700 °C, the rate-limiting step is the diffusion of oxide ions in the bulk of the electrode (corresponding to resistance R4). The other electrodes, i.e., LSNCO10 and LSNCO20, follow a similar trend in the 700–900 °C temperature range, as shown in the Supplementary Materials, Figure S4.

### 3.5.2. Impedance Data Analysis under Polarization

The electrochemical properties of the symmetrical cells were further investigated under polarization from −0.2 V to +0.2 V in order to determine the exchange current density ( $i_0$ ). Using the Butler–Volmer equation (Equation (7)), the value of the exchange current density ( $i_0$ ) can be obtained for the electrodes:

$$i = i_0 \left\{ e^{\frac{(1-\alpha)nF\eta}{RT}} - e^{-\frac{\alpha nF\eta}{RT}} \right\} \quad (7)$$

where  $i$  is the current density,  $\eta$  is the overpotential,  $n$  is the number of electrons transferred in the charge transfer reaction, and  $\alpha$  is a measure of the symmetry between the oxidative and reductive processes. Evaluating the Butler–Volmer equation through high field approximation ( $|\eta| > 0.1$  V) yields the Tafel equation below (Equation (8)).

$$\ln|i| = \ln|i_0| - \frac{\alpha F\eta}{RT} \quad (8)$$

The Tafel plot is then obtained by plotting the  $\log|i|$  as a function of  $\eta$ , while the value of the  $i_0$  is evaluated from the intercept of the plot [51,52]. The impedance spectra under polarizations were recorded from 700 to 900 °C with a three-electrode setup. For LSNCO5 and LSNCO10, the impedance spectra were fitted with four R//CPE along with the  $R_s$ , while for LSNCO20, the spectra were fitted using three R//CPE along with the  $R_s$ . Variation of individual resistance for LSCNCO10 and LSNCO20 as a function of polarization are shown in Figure S5, as an example. The charge transfer resistance (R2) was considered to determine the cell overpotentials ( $\eta$ ), hence the value of  $\eta$  for the charge transfer process was obtained by multiplying R2 (charge transfer resistance) with the measured current ( $i$ ). The Tafel plot was traced for LSNCO5, LSNCO10, and LSNCO20 symmetrical half-cells at



800 °C, by plotting  $\log(i)$  vs.  $\eta$  (Figure 11). It is clear that the cell overpotential is increased with increasing Sr content.

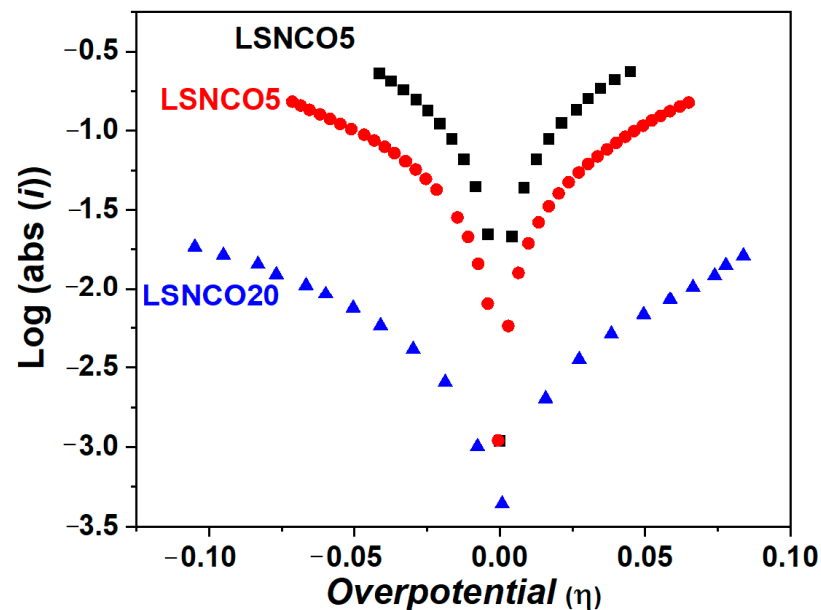


Figure 11. Variation of the Tafel plot as a function of Sr substitution at 800 °C.

Figure 12 illustrates the variation of the exchange current density ( $i_0$ ) as a function of temperature and Sr substitution. From the graph, it is observed that the exchange current density decreases with decreasing temperature. The observed trend is expected due to a decrease in the electrode's kinetic activity at lower operating temperatures. Furthermore, the exchange current density is decreasing with increasing Sr content throughout the temperature range of 700–900 °C. For instance, at 800 °C, the  $i_0$  values are 0.05, 0.03, and 0.003 A·cm<sup>-2</sup> for LSNCO5, LSNCO10, and LSNCO20, respectively. This trend further indicates that the electrode's reaction kinetics are decreased with Sr substitution.

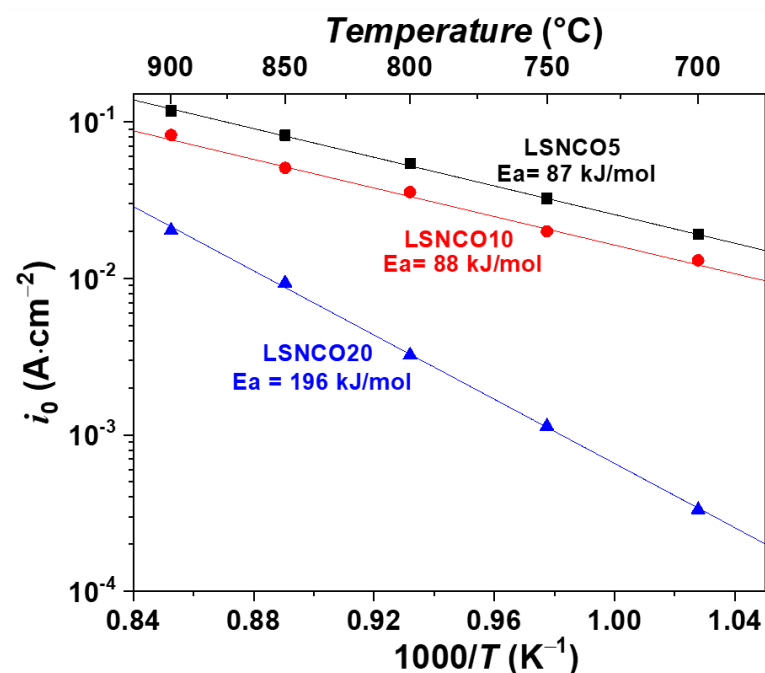


Figure 12. Variation of the exchange current density ( $i_0$ ) as a function of temperature with Sr substitution.

The decrease in overall electrode performance with Sr substitution in the LSNCO is contrary to the simple perovskites-based materials such as LSC or LSCF. In simple perovskites, the Sr substitution leads to an increase in the oxygen vacancies and a general improvement in the electrochemical processes [34,35]. However, in layered perovskites, Sr substitution in the perovskite structure decreases the interstitial sites (as seen in the TGA results), leading to a decline in the electrochemical properties. The concentration of oxygen vacancies and interstitials in the perovskite influence the kinetics of the oxygen transport through the electrode. High oxygen interstitials and vacancies offer the possibilities of fast oxygen transport due to high diffusion coefficients, and thus, a reduction in the polarization resistance of the electrode.

#### 4. Conclusions

The present study focuses on the influence of Sr substitution on the electrochemical properties of  $\text{La}_{2-x}\text{Sr}_x\text{Ni}_{0.8}\text{Co}_{0.2}\text{O}_{4+\delta}$  (LSNCO;  $0.0 \leq x \leq 0.8$ ) as oxygen electrodes in solid oxide cells. All LSNCO compositions were successfully synthesized through the modified citrate–nitrate route. The XRD pattern showed complete crystallization of the powders as single-phase in the  $\text{K}_2\text{NiF}_4$ -type orthorhombic/tetragonal structure. The increase in Sr substitution led to a decrease in lattice parameters  $a$ ,  $b$ , and  $c$ , which further led to a reduction in the lattice volume. The TGA analysis of the LSNCO powders revealed that the materials maintained reversible oxygen over stoichiometry across the considered composition ( $0 \leq x \leq 0.4$ ), from room temperature to 1000 °C in both air and oxygen atmospheres. However, the increase in the Sr-content leads to a decrease in oxygen over stoichiometry.

The electrochemical analysis of the symmetrical half-cells containing LSNCO electrodes indicates that the polarization resistance ( $R_p$ ) is increased with increasing Sr substitution. This trend is contrary to simple perovskites-based materials. In addition, the exchange current density ( $i_0$ ) is also decreased with increasing Sr content in the electrodes, which further indicates a decrease in electrode reaction kinetics. Despite lowering the reactivity between LSNCO and GDC, the performance of the cell is decreased, indicating that electrode reaction kinetics and activity are the most important parameters for the selection of suitable oxygen electrode materials. Although the initial performance of these LSNCO electrodes is lower than the LNCO electrode, it may be possible that these electrodes show a lower degradation rate during long-term operation, due to lower reactivity with GDC. Therefore, current research is being conducted to investigate the performance and long-term degradation of single cells containing LSNCO oxygen electrodes under real SOFCs and SOECs conditions.

**Supplementary Materials:** The following supporting information can be downloaded at: <https://www.mdpi.com/article/10.3390/en15062136/s1>, Figure S1: Impedance spectra of LNCO symmetrical half-cells as a function of sintering temperature (1100, 1150 and 1200 °C) under OCV conditions in air, at 700 °C; Figure S2: XRD pattern of LSNCO10 after TGA measurement under Ar-4%  $\text{H}_2$  atmosphere; Figure S3: DRT plots of (a) LSNCO5, (b) LSNCO10, and (c) LSNCO20 symmetrical half-cells at 800 °C under OCV conditions in air; Figure S4: Variation of polarization resistances of LSNCO5, LSNCO10 and LSNCO20 symmetrical half-cell as a function of  $p\text{O}_2$  at 900 and 700 °C; Figure S5: Variation of separate individual resistances as a function of applied voltage for (a) LSNCO10, and (b) LSNCO20 symmetrical half-cells at 800 °C in air.

**Author Contributions:** Conceptualization, I.D.U., V.V., I.C.V. and L.G.J.d.H.; methodology, I.D.U., V.V., I.C.V. and L.G.J.d.H.; validation, I.D.U., V.V., I.C.V. and L.G.J.d.H.; formal analysis, I.D.U. and V.V.; investigation, I.D.U. and V.V.; writing—original draft preparation, I.D.U. and V.V.; writing—review and editing, I.D.U. and V.V.; visualization, I.D.U., V.V., I.C.V. and L.G.J.d.H.; supervision, V.V., I.C.V., R.-A.E. and L.G.J.d.H.; project administration, I.C.V., R.-A.E. and L.G.J.d.H.; funding acquisition, I.C.V., R.-A.E. and L.G.J.d.H. All authors have read and agreed to the published version of the manuscript.

**Funding:** This research received no external funding.

**Institutional Review Board Statement:** Not applicable.

**Informed Consent Statement:** Not applicable.

**Data Availability Statement:** Not applicable.

**Conflicts of Interest:** The authors declare no conflict of interest that could have appeared to influence the research work. The funders had no role in the design of the study; in the collection, analyses, or interpretation of data; in the writing of the manuscript, or in the decision to publish the results.

## References

1. Chuahy, F.D.; Kokjohn, S.L. Solid Oxide Fuel Cell and Advanced Combustion Engine Combined Cycle: A Pathway to 70% Electrical Efficiency. *Appl. Energy* **2019**, *235*, 391–408. [\[CrossRef\]](#)
2. Shaheen, K.; Suo, H.; Shah, Z.; Hanif, M.B.; Hussain, Z.; Ali, S.; Liu, M.; Ma, L.; Cui, J.; Ji, Y.T.; et al. Electrochemical Performance of Multifuel Based Nanocomposite for Solid Oxide Fuel Cell. *Ceram. Int.* **2020**, *46*, 8832–8838. [\[CrossRef\]](#)
3. Bicer, Y.; Khalid, F. Life Cycle Environmental Impact Comparison of Solid Oxide Fuel Cells Fueled by Natural Gas, Hydrogen, Ammonia and Methanol for Combined Heat and Power Generation. *Int. J. Hydrogen Energy* **2020**, *45*, 3670–3685. [\[CrossRef\]](#)
4. Liu, Y.; Jia, L.; Chi, B.; Pu, J.; Li, J. In Situ Exsolved Ni-Decorated Ba(Ce<sub>0.9</sub>Y<sub>0.1</sub>)<sub>0.8</sub>Ni<sub>0.2</sub>O<sub>3-δ</sub> Perovskite as Carbon-Resistant Composite Anode for Hydrocarbon-Fueled Solid Oxide Fuel Cells. *ACS Omega* **2019**, *4*, 21494–21499. [\[CrossRef\]](#) [\[PubMed\]](#)
5. Sarruf, B.J.M.; Hong, J.E.; Steinberger-Wilckens, R.; de Miranda, P.E.V. Ceria-Co-Cu-Based SOFC Anode for Direct Utilisation of Methane or Ethanol as Fuels. *Int. J. Hydrogen Energy* **2020**, *45*, 5297–5308. [\[CrossRef\]](#)
6. Jiang, S.P. A Comparison of O<sub>2</sub> Reduction Reactions on Porous (La,Sr)MnO<sub>3</sub> and (La,Sr)(Co,Fe)O<sub>3</sub> Electrodes. *Solid State Ion.* **2002**, *146*, 1–22. [\[CrossRef\]](#)
7. Murray, E.P.; Sever, M.J.; Barnett, S.A.B. Electrochemical Performance of (La,Sr)(Co,Fe)O<sub>3</sub>–(Ce,Gd)O<sub>3</sub> Composite Cathodes. *Solid State Ion.* **2002**, *148*, 27–34. [\[CrossRef\]](#)
8. Khotseng, L. Oxygen Reduction Reaction. In *Electrocatalysts for Fuel Cells and Hydrogen Evolution—Theory to Design*; IntechOpen: London, UK, 2018.
9. Ascolani-Yael, J.; Montenegro-Hernández, A.; Garcés, D.; Liu, Q.; Wang, H.; Yakal-Kremiski, K.; Barnett, S.; Moggi, L. The Oxygen Reduction Reaction in Solid Oxide Fuel Cells: From Kinetic Parameters Measurements to Electrode Design. *J. Phys. Energy* **2020**, *2*, 042004. [\[CrossRef\]](#)
10. Yang, G.; Jung, W.; Ahn, S.J.; Lee, D. Controlling the Oxygen Electrocatalysis on Perovskite and Layered Oxide Thin Films for Solid Oxide Fuel Cell Cathodes. *Appl. Sci.* **2019**, *9*, 1030. [\[CrossRef\]](#)
11. Ren, R.; Wang, Z.; Meng, X.; Xu, C.; Qiao, J.; Sun, W.; Sun, K. Boosting the Electrochemical Performance of Fe-Based Layered Double Perovskite Cathodes by Zn<sup>2+</sup> Doping for Solid Oxide Fuel Cells. *ACS Appl. Mater. Interfaces* **2020**, *12*, 23959–23967. [\[CrossRef\]](#)
12. Huang, Y.; Ding, J.; Xia, Y.; Miao, L.; Li, K.; Zhang, Q.; Liu, W. Ba<sub>0.5</sub>Sr<sub>0.5</sub>Co<sub>0.8-χ</sub>Fe<sub>0.2</sub>Nb<sub>χ</sub>O<sub>3-δ</sub> (X ≤ 0.1) as Cathode Materials for Intermediate Temperature Solid Oxide Fuel Cells with an Electron-Blocking Interlayer. *Ceram. Int.* **2020**, *46*, 10215–10223. [\[CrossRef\]](#)
13. Xiaokaiti, P.; Yu, T.; Yoshida, A.; Du, X.; Hao, X.; Kasai, Y.; Abudula, A.; Guan, G. Effects of Cobalt and Iron Proportions in Pr<sub>0.4</sub>Sr<sub>0.6</sub>Co<sub>0.9-χ</sub>Fe<sub>χ</sub>Nb<sub>0.1</sub>O<sub>3-δ</sub> Electrode Material for Symmetric Solid Oxide Fuel Cells. *J. Alloys Compd.* **2020**, *831*, 154738. [\[CrossRef\]](#)
14. Qiu, Y.; Li, H.; Liu, Y.; Chi, B.; Pu, J.; Li, J. Effects of Niobium Doping on the Stability of SrCo<sub>0.2</sub>Fe<sub>0.8</sub>O<sub>3-δ</sub> Cathodes for Intermediate Temperature Solid Oxide Fuel Cells. *J. Alloys Compd.* **2020**, *829*, 154503. [\[CrossRef\]](#)
15. Kim, S.J.; Choi, G.M. Stability of LSCF Electrode with GDC Interlayer in YSZ-Based Solid Oxide Electrolysis Cell. *Solid State Ion.* **2014**, *262*, 303–306. [\[CrossRef\]](#)
16. Vibhu, V.; Rougier, A.; Nicollet, C.; Flura, A.; Grenier, J.C.; Bassat, J.M. La<sub>2-χ</sub>Pr<sub>χ</sub>NiO<sub>4+δ</sub> as Suitable Cathodes for Metal Supported SOFCs. *Solid State Ion.* **2015**, *278*, 32–37. [\[CrossRef\]](#)
17. Mao, J.; Peng, S.; Zhang, C.; Qi, S.; Cui, J.; Gong, Y.; Wang, S.; Wu, C.; Zhou, Q. Electrode Properties of (Pr<sub>0.9</sub>La<sub>0.1</sub>)<sub>2-χ</sub>(Ni<sub>0.74</sub>Cu<sub>0.21</sub>Al<sub>0.05</sub>)O<sub>4+δ</sub> (with X = 0, 0.05, and 0.1) as Cathodes in IT-SOFCs. *J. Alloys Compd.* **2019**, *793*, 519–525. [\[CrossRef\]](#)
18. Montenegro-Hernández, A.; Vega-Castillo, J.; Caneiro, A.; Moggi, L. High Temperature Orthorhombic/Tetragonal Transition and Oxygen Content of Pr<sub>2-χ</sub>Nd<sub>χ</sub>NiO<sub>4+δ</sub> (X = 0, 0.3, 1, 1.7 and 2) Solid Solutions. *J. Solid State Chem.* **2019**, *276*, 210–216. [\[CrossRef\]](#)
19. Boehm, E.; Bassat, J.M.; Dordor, P.; Mauvy, F.; Grenier, J.C.; Stevens, P. Oxygen Diffusion and Transport Properties in Non-Stoichiometric Ln<sub>2-χ</sub>NiO<sub>4+δ</sub> Oxides. *Solid State Ion.* **2005**, *176*, 2717–2725. [\[CrossRef\]](#)
20. Ferchaud, C.; Grenier, J.C.; Zhang-Steenwinkel, Y.; Van Tuel, M.M.A.; Van Berkel, F.P.F.; Bassat, J.M. High Performance Praseodymium Nickelate Oxide Cathode for Low Temperature Solid Oxide Fuel Cell. *J. Power Sources* **2011**, *196*, 1872–1879. [\[CrossRef\]](#)
21. Vibhu, V.; Suchomel, M.R.; Penin, N.; Weill, F.; Grenier, J.C.; Bassat, J.M.; Rougier, A. Structural Transformations of the La<sub>2-χ</sub>Pr<sub>χ</sub>NiO<sub>4+δ</sub> System Probed by High-Resolution Synchrotron and Neutron Powder Diffraction. *Dalt. Trans.* **2019**, *48*, 266–277. [\[CrossRef\]](#) [\[PubMed\]](#)
22. Simner, S.P.; Anderson, M.D.; Engelhard, M.H.; Stewenson, J.W. Degradation Mechanisms of La–Sr–Co–Fe–O<sub>3</sub>SOFC Cathodes Electrochem. *Solid State Lett.* **2006**, *9*, A478–A481. [\[CrossRef\]](#)

23. Kim, J.Y.; Sprenkle, V.L.; Canfield, N.L.; Meinhardt, K.D.; Chick, L.A.; Benson, S.J.; Waller, D.; Kilner, J.A. Degradation of  $\text{La}_{0.6}\text{Sr}_{0.4}\text{Co}_{0.2}\text{Fe}_{0.8}\text{O}_3$  in Carbon Dioxide and Water Atmospheres. *J. Electrochem. Soc.* **1999**, *146*, 1305–1309.
24. Vibhu, V.; Yildiz, S.; Vinke, I.C.; Eichel, R.A.; Bassat, J.M.; De Haart, L.G.J. High Performance LSC Infiltrated LSCF Oxygen Electrode for High Temperature Steam Electrolysis Application. *J. Electrochem. Soc.* **2019**, *166*, F102–F108. [[CrossRef](#)]
25. Boehm, E.; Bassat, J.M.; Steil, M.C.; Dordor, P.; Mauvy, F.; Grenier, J.C. Oxygen Transport Properties of  $\text{La}_2\text{Ni}_{1-x}\text{Cu}_x\text{O}_{4+\delta}$  Mixed Conducting Oxides. *Solid State Sci.* **2003**, *5*, 973–981. [[CrossRef](#)]
26. Vibhu, V.; Vinke, I.C.; Eichel, R.A.; de Haart, L.G.J. Cobalt Substituted  $\text{Pr}_2\text{Ni}_{1-x}\text{Co}_x\text{O}_{4+\delta}$  ( $x = 0, 0.1, 0.2$ ) Oxygen Electrodes: Impact on Electrochemical Performance and Durability of Solid Oxide Electrolysis Cells. *J. Power Sources* **2021**, *482*, 228909. [[CrossRef](#)]
27. Vibhu, V.; Flura, A.; Rougier, A.; Nicollet, C.; Fourcade, S.; Hungria, T.; Grenier, J.C.; Bassat, J.M. Electrochemical Ageing Study of Mixed Lanthanum/Praseodymium Nickelates  $\text{La}_{2-x}\text{Pr}_x\text{NiO}_{4+\delta}$  as Oxygen Electrodes for Solid Oxide Fuel or Electrolysis Cells. *J. Energy Chem.* **2020**, *46*, 62–70. [[CrossRef](#)]
28. Chroneos, A.; Vovk, R.V.; Goulatis, I.L.; Goulatis, L.I. Oxygen Transport in Perovskite and Related Oxides: A Brief Review. *J. Alloys Compd.* **2010**, *494*, 190–195. [[CrossRef](#)]
29. Fu, D.; Jin, F.; He, T. A-Site Calcium-Doped  $\text{Pr}_{1-x}\text{Ca}_x\text{BaCo}_2\text{O}_{5+\delta}$  Double Perovskites as Cathodes for Intermediate-Temperature Solid Oxide Fuel Cells. *J. Power Sources* **2016**, *313*, 134–141. [[CrossRef](#)]
30. Anjum, U.; Vashishtha, S.; Agarwal, M.; Tiwari, P.; Sinha, N.; Agrawal, A.; Basu, S.; Haider, M.A. Oxygen Anion Diffusion in Double Perovskite  $\text{GdBaCo}_2\text{O}_{5+\delta}$  and  $\text{LnBa}_{0.5}\text{Sr}_{0.5}\text{Co}_{2-x}\text{Fe}_x\text{O}_{5+\delta}$  ( $\text{Ln} = \text{Gd, Pr, Nd}$ ) Electrodes. *Int. J. Hydrogen Energy* **2016**, *41*, 7631–7640. [[CrossRef](#)]
31. Vibhu, V.; Vinke, I.C.; Eichel, R.A.; Bassat, J.M.; de Haart, L.G.J.  $\text{La}_2\text{Ni}_{1-x}\text{Co}_x\text{O}_{4+\delta}$  ( $x = 0.0, 0.1$  and  $0.2$ ) Based Efficient Oxygen Electrode Materials for Solid Oxide Electrolysis Cells. *J. Power Sources* **2019**, *444*, 227292. [[CrossRef](#)]
32. Munnings, C.N.; Skinner, S.J.; Amow, G.; Whitfield, P.S.; Davidson, I.J. Oxygen Transport in the  $\text{La}_2\text{Ni}_{1-x}\text{Co}_x\text{O}_{4+\delta}$  System. *Solid State Ion.* **2005**, *176*, 1895–1901. [[CrossRef](#)]
33. Kilner, J.A.; Shaw, C.K.M. Mass Transport in  $\text{La}_2\text{Ni}_{1-x}\text{Co}_x\text{O}_{4+\delta}$  Oxides with the  $\text{K}_2\text{NiF}_4$  Structure. *Solid State Ion.* **2002**, *154–155*, 523–527. [[CrossRef](#)]
34. Kuo, J.H.; Anderson, H.U.; Sparlin, D.M. Oxidation-Reduction Behaviour of Undoped and Sr-Doped  $\text{LaMnO}_3$ : Defect Structure, Electrical Conductivity and Thermoelectric Power. *J. Solid State Chem.* **1990**, *87*, 55. [[CrossRef](#)]
35. Hammouche, A.; Schouler, E.J.L.; Henault, M.J. Electrical and Thermal Properties of Sr-Doped Lanthanum Manganites. *Solid State Ion.* **1988**, *28*, 1205. [[CrossRef](#)]
36. Courty, P.; Ajot, H.; Marcilly, C.; Delmon, B. Oxydes Mixtes Ou En Solution Solide Sous Forme Très Divisée Obtenus Par Décomposition Thermique de Précurseurs Amorphes. *Powder Technol.* **1973**, *7*, 21–38. [[CrossRef](#)]
37. Nikonov, A.V.; Kuterbekov, K.A.; Bekmyrza, K.Z.; Pavzderin, N.B. A Brief Review of Conductivity and Thermal Expansion of Perovskite-Related Oxides for SOFC Cathode. *Eurasian J. Phys. Funct. Mater.* **2018**, *2*, 274–292. [[CrossRef](#)]
38. Aguadero, A.; Escudero, M.J.; Pérez, M.; Alonso, J.A.; Pomjakushin, V.; Daza, L. Effect of Sr Content on the Crystal Structure and Electrical Properties of the System  $\text{La}_{2-x}\text{Sr}_x\text{NiO}_{4+\delta}$  ( $0 \leq x \leq 1$ ). *J. Chem. Soc. Dalt. Trans.* **2006**, *36*, 4377–4383. [[CrossRef](#)] [[PubMed](#)]
39. Bianchi, F.R.; Bosio, B.; Baldinelli, A.; Barelli, L. Optimization of a Reference Kinetic Model for Solid Oxide Fuel Cells. *Catalysts* **2020**, *10*, 104. [[CrossRef](#)]
40. Pikalova, E.Y.; Bogdanovich, N.M.; Kolchugin, A.A.; Osinkin, D.A.; Bronin, D.I. Electrical and Electrochemical Properties of  $\text{La}_2\text{NiO}_{4+\delta}$ -Based Cathodes in Contact with  $\text{Ce}_{0.8}\text{Sm}_{0.2}\text{O}_{2-\delta}$  Electrolyte. *Procedia Eng.* **2014**, *98*, 105–110. [[CrossRef](#)]
41. Sun, Q.; Chan, S.; Stempien, J. Solid Oxide Electrolyzer Cell Modeling: A Review. *J. Power Technol.* **2013**, *93*, 216–246.
42. Santaya, M.; Toscani, L.; Baqué, L.; Troiani, H.E.; Mogni, L. Study of Phase Stability of  $\text{SrTi}_{0.3}\text{Fe}_{0.7}\text{O}_{3-\delta}$  Perovskite in Reducing Atmosphere: Effect of Microstructure. *Solid State Ion.* **2019**, *342*, 3–9. [[CrossRef](#)]
43. Nagde, K.R.; Bhoga, S.S. Effect of Sr Content on Structure and Electrical Properties of  $\text{La}_{1-x}\text{Sr}_x\text{MnO}_3$  from ITSOFC Cathode View Point. *Ionics* **2009**, *15*, 571–578. [[CrossRef](#)]
44. Skinner, S.J.; Kilner, J.A. Oxygen Diffusion and Surface Exchange in  $\text{La}_{2-x}\text{Sr}_x\text{NiO}_{4+\delta}$ . *Solid State Ion.* **2000**, *135*, 709–712. [[CrossRef](#)]
45. Gao, Z.; Mogni, L.V.; Miller, E.C.; Railsback, J.G.; Barnett, S.A. A Perspective on Low-Temperature Solid Oxide Fuel Cells. *Energy Environ. Sci.* **2016**, *9*, 1602–1644. [[CrossRef](#)]
46. Inprasit, T.; Wongkasemjit, S.; Skinner, S.J.; Burriel, M.; Limthongkul, P. Effect of Sr Substituted  $\text{La}_{2-x}\text{Sr}_x\text{NiO}_{4+\delta}$  ( $x = 0, 0.2, 0.4, 0.6$ , and  $0.8$ ) on Oxygen Stoichiometry and Oxygen Transport Properties. *RSC Adv.* **2015**, *5*, 2486–2492. [[CrossRef](#)]
47. Li, W.; Guan, B.; Zhang, X.; Yan, J.; Zhou, Y.; Liu, X. New Mechanistic Insight into the Oxygen Reduction Reaction on Ruddlesden-Popper Cathodes for Intermediate-Temperature Solid Oxide Fuel Cells. *Phys. Chem. Chem. Phys.* **2016**, *18*, 8502–8511. [[CrossRef](#)]
48. Escudero, M.J.; Aguadero, A.; Alonso, J.A.; Daza, L. A Kinetic Study of Oxygen Reduction Reaction on  $\text{La}_2\text{NiO}_4$  Cathodes by Means of Impedance Spectroscopy. *J. Electroanal. Chem.* **2007**, *611*, 107–116. [[CrossRef](#)]
49. Sun, L.P.; Li, Q.; Zhao, H.; Hao, J.H.; Huo, L.H.; Pang, G.; Shi, Z.; Feng, S. Electrochemical Performance of  $\text{Nd}_{1.93}\text{Sr}_{0.07}\text{CuO}_4$  Nanofiber as Cathode Material for SOFC. *Int. J. Hydrogen Energy* **2012**, *37*, 11955–11962. [[CrossRef](#)]
50. Kolchugin, A.A.; Pikalova, E.Y.; Bogdanovich, N.M.; Bronin, D.I.; Filonova, E.A. Electrochemical Properties of Doped Lanthanum-Nickelate-Based Electrodes. *Russ. J. Electrochem.* **2017**, *53*, 826–833. [[CrossRef](#)]

- 
51. Hotza, S.; Gomez, S.Y. Solid Oxide Electrolysers. In *Electrochemical Methods for Hydrogen Production*; Keith, S., Ed.; The Royal Society of Chemistry: London, UK, 2020; pp. 136–174.
  52. Chen, Z.; Hassan, F.M.; Yu, A. Electrochemical Engineering Fundamentals. *Electrochem. Technol. Energy Storage Convers.* **2012**, *1*, 45–68.